

The Information Content of Projected Galaxy Fields

Lucas Porth ^{1,2,3*}, Gary M. Bernstein ^{2†}, Robert E. Smith ¹, Abigail J. Lee ^{2,4}

¹*Astronomy Centre, Department of Physics & Astronomy, University of Sussex, Brighton, BN1 9RH, UK*

²*Department of Physics & Astronomy, University of Pennsylvania, Philadelphia, PA 19104, USA*

³*Argelander-Institut für Astronomie, Universität Bonn, Auf dem Hügel 71, 53121 Bonn, Germany*

⁴*Department of Astronomy & Astrophysics, University of Chicago, 5640 South Ellis Avenue, Chicago, IL 60637*

Accepted XXX. Received YYY; in original form ZZZ

ABSTRACT

The power spectrum of the nonlinearly evolved large-scale mass distribution recovers only a minority of the information available on the mass fluctuation amplitude. We investigate the recovery of this information in 2D “slabs” of the mass distribution averaged over $\approx 100 h^{-1}\text{Mpc}$ along the line of sight, as might be obtained from photometric redshift surveys. We demonstrate a Hamiltonian Monte Carlo (HMC) method to reconstruct the non-Gaussian mass distribution in slabs, under the assumption that the projected field is a point-transformed Gaussian random field, Poisson-sampled by galaxies. When applied to the *Quijote* N -body suite at $z = 0.5$ and at a transverse resolution of $2 h^{-1}\text{Mpc}$, the method recovers ~ 30 times more information than the 2D power spectrum in the well-sampled limit, recovering the Gaussian limit on information. At a more realistic galaxy sampling density of $0.01 h^3\text{Mpc}^{-3}$, shot noise reduces the information gain to a factor of five improvement over the power spectrum at resolutions of $4 h^{-1}\text{Mpc}$ or smaller.

Key words: cosmology: large-scale structure of Universe. – methods: numerical

1 INTRODUCTION

The potential constraining power of cosmological large-scale-structure surveys depends, at root, on the observed area and on the survey depth. As a theoretical description of the nonlinear density field is lacking, the full information cannot be retrieved and instead one performs cosmological analyses with the help of summary statistics. The most widely used statistic is the power spectrum, which captures the available information only for Gaussian fields. In the context of 3D fields (Neyrinck et al. 2009, 2011; Simpson et al. 2013) and the cosmic convergence field (Joachimi et al. 2011; Seo et al. 2011; Simpson et al. 2016; Giblin et al. 2018) linearization and clipping methods have been proposed that successfully remap some of the nonlinear information into the second order statistics. However the information gain can be strongly depleted once shot noise is taken into account. A more complete way to extract cosmological information from spectroscopic surveys can be formulated in terms of forward modelling approaches that do not need to compress the observed data. In particular the proposed models in Kitaura & Enßlin (2008); Jasche & Kitaura (2010); Jasche & Wandelt (2013); Wang et al. (2014) and Jasche et al. (2015) have been successfully applied to N -body simulations and real galaxy redshift surveys (Lavaux & Jasche 2016; Leclercq et al. 2017) to reveal a wealth of information of the dark matter density field and its phase space distribution in our nearby Universe. Due to the high dimensionality of the resulting posteriors, those models have mainly been used to reconstruct 3D cosmic fields when using a fixed cosmology. Recently the joint sam-

pling of cosmology and fields has gained more traction (Leclercq & Heavens 2021; Porqueres et al. 2021).

In this work we aim to test how well an idealized forward model performs for *projected* tracer fields with a line-of-sight resolution of $\Delta\chi \approx 100 h^{-1}\text{Mpc}$, such as might be acquired from imaging surveys using photometric redshifts. To assess the information contained in the resulting posterior we do not keep the cosmology fixed and allow the amplitude of the transformed power spectrum to vary. The information content can then be rephrased as the signal-to-noise (squared) of the estimated amplitude parameter after having marginalized over the projected mass field itself.

This paper is organised as follows: In §2 we introduce the hierarchical model adopted for our reconstruction and test the validity of our parametrizations on the *Quijote* simulation suite (Villaescusa-Navarro et al. 2020). In §3 we give an overview of the Hamiltonian Monte Carlo sampling algorithm and lay out some specific choices we made for our implementation. In §4 we first validate our model on a suite of lognormal simulations, then apply it to the *Quijote* suite and finally compare the reconstruction confidence intervals of the hierarchical model to the expected signal-to-noise using standard 2-point analysis methods. In §5 we summarize our findings, conclude and discuss future work.

2 MODEL

For this work we suppose that we are given a set of galaxies on a two dimensional plane. We then cover the plane with a regular grid and assign the galaxies to the grid cells, yielding a set of galaxy counts $N \equiv \{N_c\}$. A hierarchical model connecting the observations

* E-mail: lporth@uni-bonn.de

† E-mail: garyb@physics.upenn.edu

to a Gaussian mass field δ^{lin} with a (projected) power spectrum¹ P parametrized by a set of parameters Π_P can then be schematically written as:

$$\begin{aligned} \mathbb{P}(\delta^{\text{lin}}, \Pi_P, \Pi_B, \Pi_G | N) \\ \propto \int d\delta^{\text{nl}} \mathbb{P}(N | \delta^{\text{nl}}, \Pi_B) \mathbb{P}(\delta^{\text{nl}} | \delta^{\text{lin}}, \Pi_G) \\ \times \mathbb{P}(\delta^{\text{lin}} | \Pi_P) \mathbb{P}(\Pi_P) \mathbb{P}(\Pi_B, \Pi_G), \end{aligned} \quad (1)$$

where δ^{nl} denotes a nonlinear mass field for which the galaxies are assumed to be biased tracers and G is a gaussianization operator with parameters Π_G that maps δ^{nl} to δ^{lin} . The model for galaxy bias is encoded in a bias operator B with parameters Π_B . In the following we will give our modelling choices for each contribution to Eq. (1).

The Poissonian likelihood

The first term models the way on how the set of discrete tracers is sampled onto the dark matter fluid, we assume this to follow an inhomogeneous Poisson process (Layzer 1956; Peebles 1980):

$$\mathbb{P}(N | \delta^{\text{nl}}, B, \bar{n}) = \mathbb{P}(\bar{n}) \prod_c e^{-n_c V} \frac{(n_c V)^{N_c}}{N_c!}, \quad (2)$$

$$n_c \equiv \bar{n} \left(1 + B[\delta^{\text{nl}}]_c\right), \quad (3)$$

where the intensity is given by the galaxy density field n which depends on the mean number density of observed galaxies \bar{n} and on the physical connection B between the galaxies and dark matter. The product of the intensity with the underlying voxel volume V then gives the expected number of galaxies in the corresponding pixel. Furthermore, we put a logarithmic prior on \bar{n} , such that one can perform an analytic marginalization:

$$\begin{aligned} \mathbb{P}(N | \delta^{\text{nl}}, B) \\ \propto \int \frac{d\bar{n}}{\bar{n}} \prod_c e^{-n_c V} \frac{(n_c V)^{N_c}}{N_c!} \\ \propto \prod_c \left(1 + B[\delta^{\text{nl}}]_c\right)^{N_c} \int d\bar{n} \bar{n}^{N_{\text{tot}}-1} e^{-\bar{n} V \sum_c (1+B[\delta^{\text{nl}}]_c)} \\ \propto \left\{ \sum_c \left(1 + B[\delta^{\text{nl}}]_c\right) \right\}^{-N_{\text{tot}}} \prod_c \left(1 + B[\delta^{\text{nl}}]_c\right)^{N_c}, \end{aligned} \quad (4)$$

where N_{tot} denotes the total number of observed tracers. With the galaxy counts N as the only observables, there is a degeneracy between the gaussianization function G and the bias functional B . For this paper we will therefore assume the identity $B(\delta) = \delta$, and we construct a ‘‘galaxy’’ catalog by Poisson sampling of the true mass distribution. In future work we will consider the combination of galaxy-count and weak-lensing observables, which will permit introduction of non-trivial bias, and a distinction between the mass and galaxy fields.

Gaussianization function

The second term in Eq. (1) corresponds to a physical model that evolves a linear density field to a nonlinear one. For this work we

will assume a deterministic point transformation model of structure formation, such that

$$\mathbb{P}(\delta^{\text{nl}} | \delta^{\text{lin}}, \Pi_G) = \prod_c \delta^D \left[\delta_c^{\text{nl}} - G^{-1}(\delta_c^{\text{lin}}, \Pi_G) \right], \quad (5)$$

where G is a function that aims at inverting structure formation. For this work we will consider two different forms of G^{-1} . The first is a logarithmic transformation, while the second one (which we dub DoubleLog) interpolates between two exponentials:

Logarithmic :

$$G^{-1}(\delta^{\text{lin}}) = e^{\delta^{\text{lin}} - \sigma^2/2} - 1; \quad (6)$$

DoubleLog :

$$G^{-1}(\delta^{\text{lin}}) = n e^{a_1 \delta^{\text{lin}} - a_1^2 \sigma^2/2} \left(1 + e^{(\delta^{\text{lin}} - \delta_0)t}\right)^{\frac{a_2 - a_1}{t}} - 1 \quad (7)$$

$$= n' e^{\frac{a_1 + a_2}{2} \delta^{\text{lin}}} \cosh\left[(\delta^{\text{lin}} - \delta_0)t/2\right]^{\frac{a_2 - a_1}{t}} - 1 \quad (8)$$

where σ^2 is the variance of the linear overdensity field and the normalization constants n and n' are defined to yield $\langle \delta^{\text{nl}} \rangle \equiv 0$. Note that the DoubleLog transformation is constructed to interpolate between two biased logarithmic transformations around a characteristic scale δ_0 with a transition width described by $1/t$. For the logarithmic transformation there are no free parameters Π_G once the linear field’s variance σ^2 is specified. For the DoubleLog function, $\Pi_G = \{\alpha_1, \alpha_2, \delta_0, t\}$.

The Gaussian prior

Assuming that the function G completely gaussianizes the δ^{nl} , the linear field will be fully described by its correlation function ξ , which depends on Π_P , such that we can write down a corresponding prior as

$$\mathbb{P}(\delta^{\text{lin}} | \Pi_P) = \frac{1}{\sqrt{(2\pi)^{n_{\text{pix}} |\xi|}}} \exp\left[-\frac{1}{2} \sum_{c,c'} \delta_c^{\text{lin}} \xi_{cc'}^{-1} \delta_{c'}^{\text{lin}}\right], \quad (9)$$

where n_{pix} denotes the total number of pixels in the grid and $|\xi|$ is the determinant of the correlation matrix. In order to circumvent the computationally infeasible operations in this representation we evaluate the determinant and the convolution in Eq. (9) in its harmonic basis indexed by a wavevector k :

$$\mathbb{P}(\delta^{\text{lin}} | P(\Pi_P)) \propto \left(\prod_k P_k^{-1/2}\right) \exp\left[-\sum_k \frac{|\widehat{\delta^{\text{lin}}}_k|^2}{2P_k}\right]. \quad (10)$$

For the remainder of this work we will assume that P is parametrizable by a function that interpolates between two different power laws, with $\Pi_P = \{A, k_0, a_1, a_2, s\}$:

$$P(k; \Pi_P) = A \left(\left(\frac{k}{k_0}\right)^{a_1 s} + \left(\frac{k}{k_0}\right)^{a_2 s} \right)^{-\frac{1}{s}}. \quad (11)$$

The parameters k_0 and s determine the location and sharpness of the power-law transition.

Accuracy of parametrizations

For assessing the applicability of the parametrizations Eq. (7) and Eq. (11) to N-body simulations we test their accuracy with help of the Quijote suite. In particular, we make use of the ensemble of 100 high resolution simulations in which 1024^3 particles were evolved within

¹ Throughout this work we will refer to the volume normalised, projected power spectrum as the power spectrum.

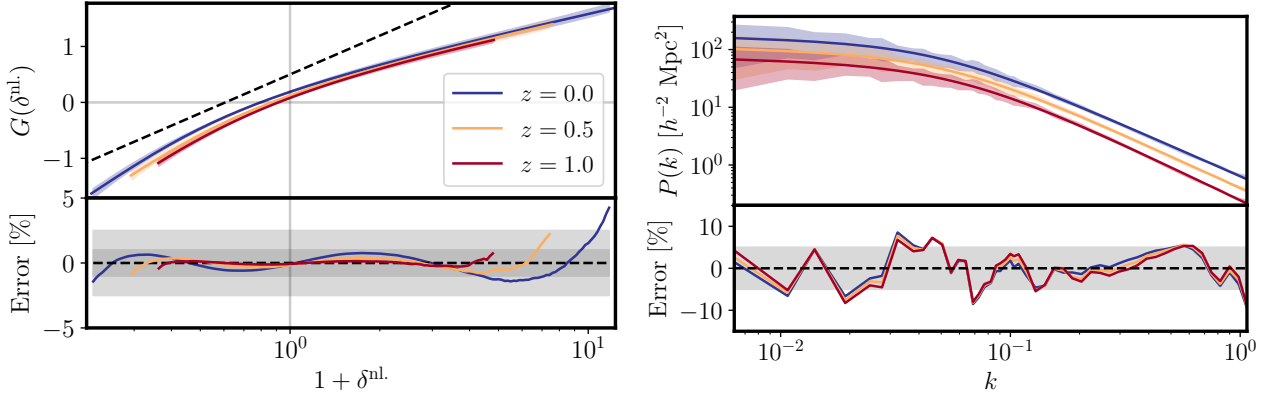


Figure 1. *Left hand side:* Gaussianizing transformations for a transverse resolution of $\approx 4 h^{-1} \text{Mpc}$ for the three redshifts probed in this work. The shaded region in the upper panel corresponds to the standard deviation of the numerical transformation equations across the ensemble. The solid lines in the upper panel correspond to the best fit model Eq. (7). The black dashed line indicates the expected scaling from a logarithmic transformation model Eq. (6). The lower panel displays the relative error between the best fit model and the mean numerical transformation with the shaded regions displaying the 2% and 1% errorbands, respectively. *Right hand side:* Same as the plot on the left, but for the power spectra of the transformed fields. In the lower panel we plot the 5% errorband. In order to make the curves appear smooth the high- k regime we switch to a logarithmic binning at these scales.

a $1 h^{-1} \text{Gpc}$ box. After retrieving the snapshots at $z \in \{1, 0.5, 0\}$ we assign the particles onto a regular mesh consisting of 256^3 voxels using a NGP scheme. From those we create projected mass fields by specifying a projection depth and summing up the content in the corresponding voxels.

For each mass slab i we then employ inverse transform sampling to construct a linearising function G_i^{num} that maps the projected overdensity field to a field following a Gaussian distribution with zero mean and a variance matching the one we would have obtained when log-transforming the overdensity field. Averaging over all the G_i^{num} defines our numeric gaussianizing function G^{num} to which we fit the DoubleLog transformation Eq. (7). The best fit parameters then determine our model for G^{-1} . The results from this procedure for our chosen angular resolution of $\approx 4 h^{-1} \text{Mpc}$ and a projection depth of $\approx 100 h^{-1} \text{Mpc}$ are shown in the left panel of Fig. 1 and we see that G does give a percent-accurate fit for nearly all pixels. We furthermore note that while G scales similarly to a logarithmic model around the mode of δ^{nl} , it does quite strongly deviate from such a model for moderately overdense and underdense regions.

After having fixed the linearization procedure we transform each of the projected overdensity fields according to G and compute the associated power spectra P_i . Again, we determine the best fit parameters of the model Eq. (11) against the mean of the P_i to define our final model for P . We show the numeric result in the right hand side of Fig. 1. As for the transformations we find a reasonable agreement across all scales. Repeating the analysis described above for different transverse resolutions of approximately 16, 8 and $2 h^{-1} \text{Mpc}$, as well as for power spectrum fits to models where the logarithmic transformation Eq. (6) had been applied we find that in all cases the chosen parametrizations provide a good enough fit for the main goal of this paper, i.e. to reasonably assess the information contained in the hierarchical model Eq. (1). We postpone a more thorough modelling of the power spectrum (i.e. by including BAO features or by directly linking it to differentiable Boltzmann codes) to future work.

3 SAMPLING METHOD

3.1 Hamiltonian Monte Carlo Sampling

We employ a Hamiltonian Monte Carlo (HMC) scheme (Duane et al. 1987) to efficiently sample from the high dimensional distribution in Eq. (1). This method evades the curse of dimensionality by exploring level sets of a distribution $\mathcal{P} \propto e^{-\mathcal{H}}$ in which the Hamiltonian \mathcal{H} is defined as

$$\mathcal{H}(\vec{q}, \vec{p}) \equiv \frac{1}{2} \vec{p}^T \mathbf{M}^{-1} \vec{p} + \psi(\vec{q}); \quad (12)$$

$$\psi(\vec{q}) \equiv -\ln \mathbb{P}(\vec{q}), \quad (13)$$

where we assume the auxiliary momentum variables \vec{p} to follow a Gaussian distribution, $\vec{p} \sim \mathcal{G}(0, \mathbf{M})$. From this formulation one can construct a valid Markov chain for the original posterior \mathbb{P} by marginalizing over the momenta and for each drawn sample of \vec{p} evolve the system to a new location (\vec{q}', \vec{p}') in phase space according to the Hamilton equations of motion

$$\begin{aligned} \frac{d\vec{q}}{dt} &= \frac{\partial \mathcal{H}}{\partial \vec{p}} = \mathbf{M}^{-1} \vec{p} \\ \frac{d\vec{p}}{dt} &= -\frac{\partial \mathcal{H}}{\partial \vec{q}} = -\nabla_{\vec{q}} \psi(\vec{q}). \end{aligned} \quad (14)$$

Due to numerical inaccuracies the Hamiltonian will not be exactly conserved along the trajectories. Thus, in order to still satisfy the detailed balance condition one then needs to invoke a Metropolis-Hastings rejection step prior to updating the chain with the value of \vec{q}' . For more complete reviews of HMC see e.g. Neal (2012).

Adopting the HMC framework to the posterior Eq.(1) we have $\vec{q} = \{\delta^{\text{lin}}, \Pi_P\}$ and by making use of Eqs.(10) and (4) the

potential ψ becomes

$$\psi(\vec{q}) = \psi_{\text{Pois}}(\delta^{\text{lin}}) + \psi_{\text{Gauss}}(\delta^{\text{lin}}, \Pi_{\mathcal{P}}); \quad (15)$$

$$\psi_{\text{Pois}} = N_{\text{tot}} \log \left[\sum_c \left(1 + G^{-1}(\delta_c^{\text{lin}}) \right) \right] - \sum_c N_c \ln \left(1 + G^{-1}(\delta_c^{\text{lin}}) \right); \quad (16)$$

$$\psi_{\text{Gauss}} = \frac{1}{2} \sum_k \left(\ln(P_k) + \frac{|\widetilde{\delta_{\text{lin},k}^{\text{lin}}}|^2}{P_k} \right). \quad (17)$$

3.2 Implementation specifics

As for all sampling schemes there exist multiple knobs that need to be tweaked in order to facilitate an efficient exploration of our posterior. In this subsection we give a top-level overview of the choices for our implementation and refer the reader to Appendix A for more details.

To avoid performing a computationally infeasible number of $O(N_c^2)$ steps in the implementation of Eq. (14), it is essential that the mass matrix \mathbf{M} takes a sparse form in a readily accessible basis. For efficiency of the HMC chain, i.e. weakly correlated samples, \mathbf{M} should approximate the Hessian of Eq. (1). Our most efficient solution is sparse in harmonic space and it allows for sampling of complex momenta from $\mathcal{G}(0, \mathbf{M})$ at computational complexity bound by FFT operations at $O(N_c \log N_c)$, as well as for $O(N_c)$ complexity for the matrix vector product in Eq. (14). We note that employing a diagonal mass matrix associated with the Hessian of the Gaussian part of the potential gave similarly good convergence properties.

As advocated by the standard literature we implement a leapfrog integrator to discretise the evolution equations Eq. (14). This method is expected to be effective as it is a second order symplectic discretization scheme that will conserve the Hamiltonian for a well chosen step-size. We also check whether some versions of higher order symplectic integrators (see Creutz & Gocksch (1989); Yoshida (1990); McLachlan (1995) for the original formulations, or Hernández-Sánchez et al. (2021) for a first application to cosmology) result in an effective speedup; while for models using a fixed cosmology the leapfrog integrator remains the most efficient routine we find that for models with varying cosmology the fourth order integrator of McLachlan (1995) yields the largest effective sample size per unit time.

In order to choose a useful step-size for the integrator we apply a dual averaging scheme (Nesterov 2009; Hoffman & Gelman 2014) during the burn-in stage that iteratively adapts the step-size to a value that will result in some specified acceptance rate δ during the sampling phase. Once burn-in is over we fix the step-size to its final value ϵ in the iteration.

Due to the high dimensionality of the problem we also need to worry about the memory footprint of the chain outputs. In this work we are mainly concerned with the chains of the power spectrum parameters $\Pi_{\mathcal{P}}$ and therefore we save those as a whole, but we save the latent field parameters δ^{lin} of only a fraction of the pixels. As the convergence properties of the δ_c^{lin} depend on the number of tracers in the corresponding pixel we make sure that our selection does include sufficiently many overdense and underdense regions. For assessing the convergence of the latent field in harmonic space we additionally store a representative selection of chains in this basis.

4 RESULTS

4.1 General strategy

For the remainder of this work we will solely concern ourselves with models \mathcal{M} that vary the power spectrum amplitude A jointly with the cosmological field δ^{lin} and fix the remaining power spectrum parameters to their best-fit values. We furthermore introduce a nominal value A^* for the power spectrum amplitude that is used to build the mass matrix. The nominal value is related to the best-fit value A^{f} of the amplitude as $A^* = \beta A^{\text{f}}$, where in our case we let $\beta \in [2/3, 3/2]$. We can then take A^* to be the initial value A_0 for the amplitude in the chain. A possible starting position of the latent field, δ_0^{lin} , can be chosen as a random Gaussian field constructed to match the true power spectrum with a strongly reduced amplitude.

When running the model \mathcal{M} with these initial conditions we found that the burn-in period becomes very prolonged as the starting point is in strong conflict with the Poisson likelihood and a very small step-size becomes necessary to navigate the chains to their stationary territory². To circumvent most of the complexity we adopt a nested burn-in strategy where in a first step we run a simpler model \mathcal{M}' in which we also fix $A \equiv A^*$. Burning in this model with δ_0^{lin} is fast and choosing some sample from \mathcal{M}' once stationarity is reached yields a better starting configuration δ_0^{lin} for the full model \mathcal{M} that does not burn in much quicker.

Additionally, we note that our procedures for generating mock data, as well as the sampling procedure, are stochastic and are drawn according to some random seeds r for each chain:

- (i) The cosmic initial condition r_{cosmo} that gives rise to ‘true’ projected density field, i.e. which realization and spatial ‘slab’ of the Quijote simulation are used;
- (ii) The Poisson sampling process r_{Pois} that selects ‘galaxies’ from the mass distribution;
- (iii) The r_{ini} used to initialize δ^{lin} in the reconstruction algorithm;
- (iv) The r_{mom} for the Markov chain, i.e. the draws from the multivariate normal momentum distribution, and for the Metropolis rejection step.

If we want to make a solid prediction about the information content in the power spectrum amplitude A we would formally need to marginalize over a large set of seed configurations. We can get rid of one dimension when making the assumption that r_{ini} and r_{mom} do not influence each other, and we collect both seeds in a new one, r_{hmc} . Checking the dispersion of the outcomes when varying over r_{hmc} for fixed r_{cosmo} and r_{Pois} is then equivalent to assessing the convergence property of the chains, i.e. by virtue of the Gelman-Rubin diagnostics (Gelman & Rubin 1992). Varying over the remaining two seeds is necessary and we do this for our analysis.

4.2 Validation on lognormal simulations

While the point transformations G do a good job in removing nonlinearities of the mass field, they are not sufficient to fully gaussianize the field, which renders the prior Eq. (10) formally incorrect. In order to test our implementation we apply it to an ensemble of mock catalogs drawn from truly lognormal mass distributions. In particular, we obtain a tracer realization as follows:

- (i) We specify a resolution and spatial extent of the slab, as well as a tracer sampling density \bar{n} ;

² We tried various other initialization choices for δ_0^{lin} and A_0 . For each of them we found the same pathological behaviour.

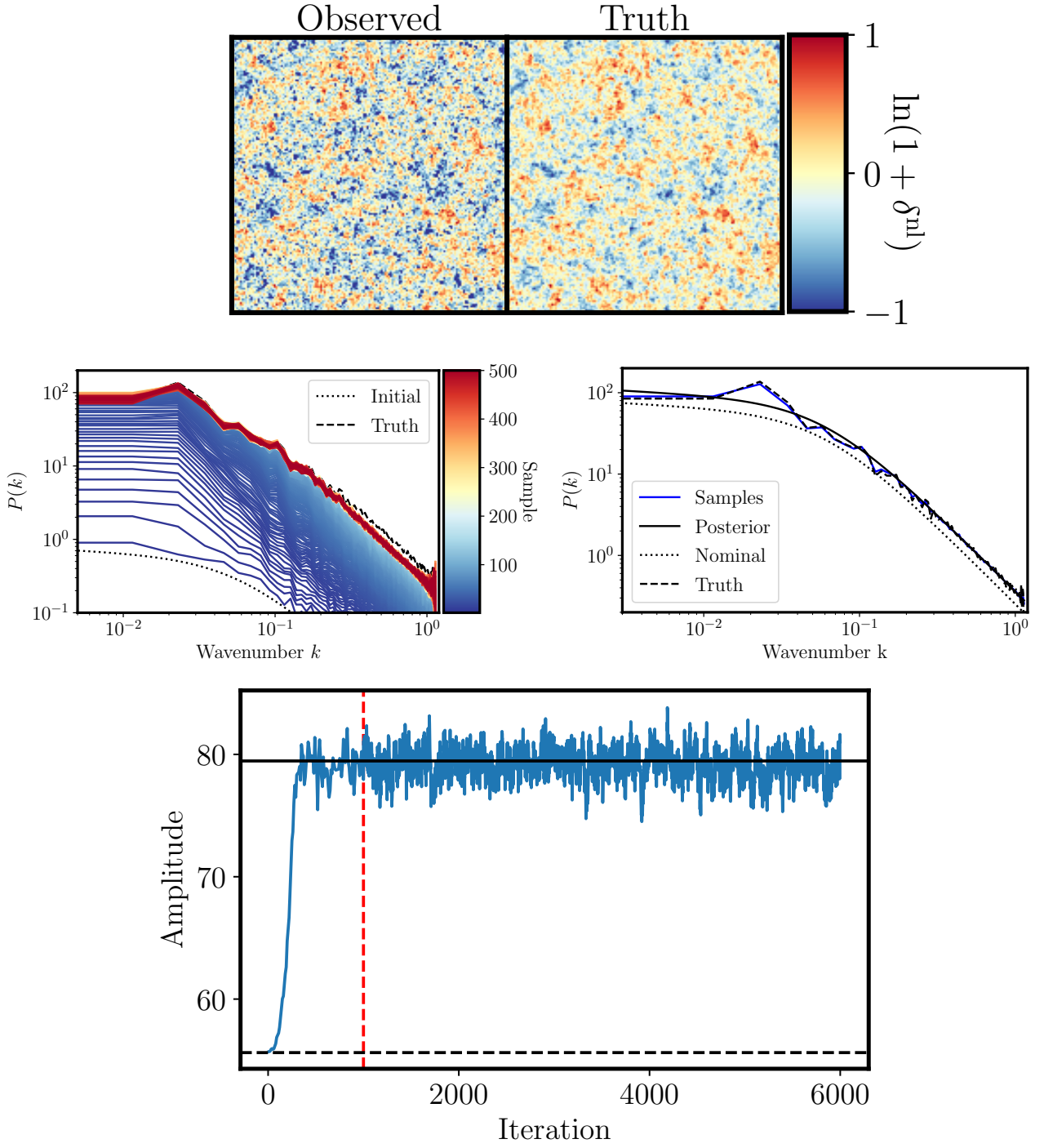


Figure 2. Sampling of the posterior Eq. (1) on a lognormal mock catalog. *Upper panel:* Comparison of the observed galaxy field to the underlying true field. *Middle left panel:* Power spectra of the proposed latent fields during burn-in of the simplified model \mathcal{M}' . *Middle right panel:* Results of the sampling stage when using the full model \mathcal{M} . The blue errorband indicates the variance of the power spectra measured from the proposed latent fields whereas the black solid line gives evaluates the theoretical power spectrum model with the mean of the proposed values for the amplitude. *Lower panel:* The amplitude chain of the model \mathcal{M} during the burn-in stage (left of the red dashed line) and the sampling stage. The solid black line indicates the value A^f that was used for generating the mock data while the dashed black line indicates the nominal value $A^* = 0.7A^f$.

Name	Nside	Depth [Δ_{pix}]	G^{-1}	Snapshots	Poisson realizations	Tracer densities	Initial conditions
DoubleLog_HighRes	512	50	DoubleLog	5	4	4	6
DoubleLog_BaseRes	256	25	DoubleLog	100	4	4	8
DoubleLog_LowRes	128	12	DoubleLog	5	8	4	6
DoubleLog_vLowRes	64	6	DoubleLog	5	8	4	6
Log_HighRes	512	50	Log	5	4	4	6
Log_BaseRes	256	25	Log	5	4	4	6
DoubleLog_HighRes_mcl	512	50	DoubleLog	10	4	5	6
DoubleLog_BaseRes_mcl	256	25	DoubleLog	10	4	5	6
DoubleLog_LowRes_mcl	128	12	DoubleLog	10	4	5	6
DoubleLog_vLowRes_mcl	64	6	DoubleLog	10	4	5	6
Log_BaseRes_mcl	256	25	Log	10	4	5	6
DoubleLog_BaseRes_lf	256	25	DoubleLog	10	4	5	6

Table 1. Parameter settings for the various ensemble runs at $z = 0.5$ performed on snapshots from the Quijote simulation suite. For each of the chains the four tracer densities that are varied over are 0.002, 0.005, 0.01, and 1.0 tracers per inverse $h^{-3}\text{Mpc}^3$. The DoubleLog_BaseRes run probes the whole Quijote ensemble and consists of the most ($100 \times 4 \times 4 \times 8 = 12800$) individual chains. Each chain consists of 5000 Hamiltonian samples. The first six runs are set up according to the description in the main text while for the latter six we use a more restrictive value of δ in the dual averaging algorithm. The last of those is performed using the standard leapfrog integrator while for all the other runs we use the fourth order symplectic integrator of McLachlan (1995). We do furthermore repeat the DoubleLog_<resolution>_mcl runs for redshifts of $z \in \{0, 1\}$.

(ii) We generate a 2d Gaussian random field g having a power spectrum P_g that is tuned to match the best-fit power spectrum of the Quijote ensemble of the corresponding slab specifics;

(iii) We generate a lognormal field as δ^{ln} by applying the transformation Eq. (6) to g ;

(iv) We Poisson-sample tracer “galaxies” into the pixels

As an example, we show in Fig. 2 the results of a single chain run on a 256^2 grid. Here, we chose to evolve the system for 40 time steps before updating the chain³. Furthermore, we set $\beta \equiv 0.7$ and choose $\bar{n} \equiv 0.005 h^3\text{Mpc}^{-3}$. Looking at the first burn-in stage, using the model \mathcal{M}' , we see that the latent field has burned in to the nominal power spectrum after around 100 iterations. Moving to the full model \mathcal{M} we see that two measures of the power spectrum—the spectra of the latent δ^{lin} fields of the samples, and the values of amplitude A at each sample—give results that are consistent with each other and with the true mass field. During the burn-in stage of \mathcal{M} , the chain of the amplitude A evolves from the nominal value to the true amplitude that was used for generating the mock data⁴. After burn-in has finished the chain oscillates around the true value A^{f} and provides an unbiased estimate.

4.3 Application to the Quijote simulation suite

Overview of ensemble runs

We now turn to the runs on the Quijote ensemble. As discussed in §4.1, we vary cosmological ensembles, as well as Poisson sampling realizations. Additionally, we aim to investigate how the reconstruction confidence of our model is affected by the pixel resolution and the sampling density of tracers. In Table 1 we summarize the configuration details for each analysis used in this work.

For each chain we adopt the nested burn-in strategy: we sample from model \mathcal{M}' for 500 times before switching to \mathcal{M} which we burn in for another 1000 steps after which the 5000 samples that will be used for the subsequent analysis are generated. In order to obtain a new sample we evolve the equations of motion Eq. (14) for 40 (jittered) time steps. To test the convergence of the chains we furthermore save the full chains for around 5 – 20 per cent of the latent field pixels, depending on the grid resolution.

Reconstruction accuracy

Before moving to the results of the ensemble we show in Fig. 3 the real-space latent field reconstructions of a single chain when using the DoubleLog transformation Eq. (7) or the logormal one, Eq. (6).

³ In order ensure detailed balance and to avoid resonant behaviour we first decide whether to integrate forward or backward in time and then uniformly pick a sample from the resulting trajectory. We postpone the investigation of more thorough schemes (see i.e. Betancourt (2016) or Appendix A of Betancourt (2017)) that take into account the numerical inaccuracies of the symplectic integrators when selecting the trajectory to future work.

⁴ We note that for this example we use a less efficient step-size adaptation algorithm to explicitly showcase the evolution of the amplitude from the prior to the truth.

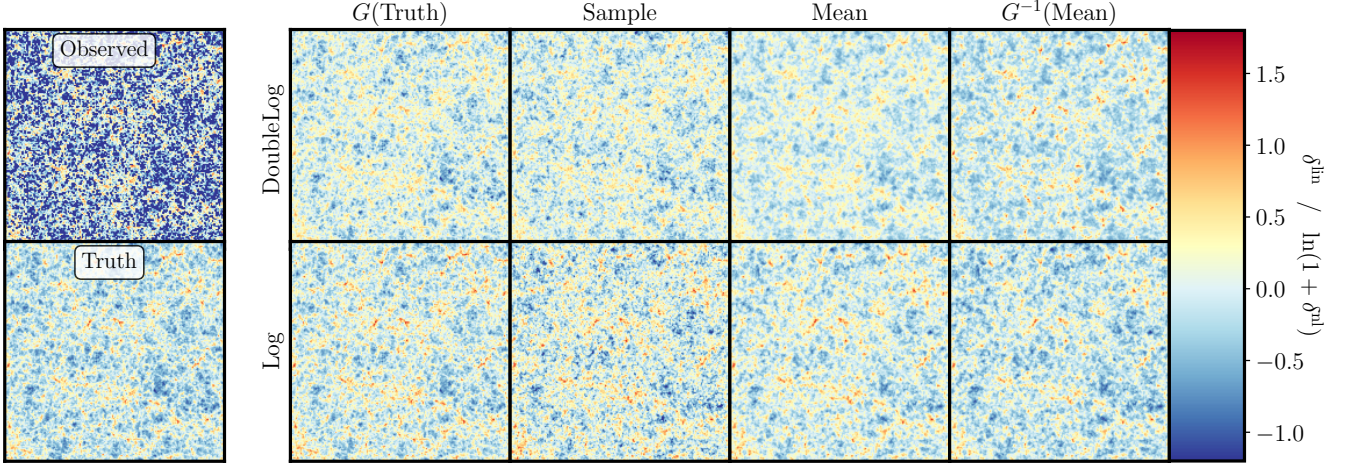


Figure 3. Latent field reconstruction on a Quijote slab using the base resolution. The leftmost plots show the observed tracer counts (top) and the underlying true mass field (bottom). In remaining panels show various measurements obtained from running the reconstruction using the DoubleLog transformation (top) or the lognormal transformation (bottom). In particular, the columns display the linearized true mass field (first), a sample from the chain (second), and the mean of all samples for the linear (third) and nonlinear (fourth) fields. For both runs we chose $\bar{n} = 0.002 h^3 \text{Mpc}^{-3}$ and matched all the random seeds.

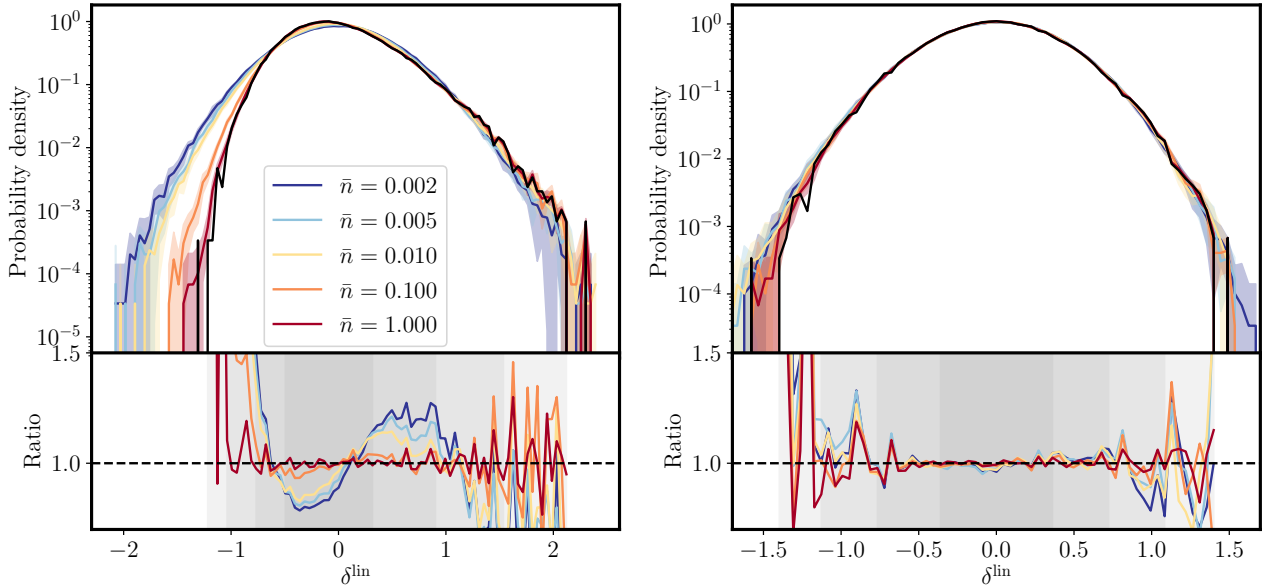


Figure 4. Reconstruction accuracy of the one point pdf of the linear density field when using the logarithmic (left) or DoubleLog (right) transformation equation. The upper panels show the linearized true mass field (black solid line), as well as the range of latent field one point distribution that are predicted by our forward model when using different sampling densities of tracers (colored lines + error bands). The bottom panels show the ratio between the true and the reconstructed pdfs and the vertical grey bands display the intervals in which 68, 95, 99.7 and 99.95 per cent of the true data resides.

We see that, as expected, neither point transformation removes the filamentary structure, and the latent δ^{lin} are not Gaussian fields. The DoubleLog model does, however, produce a more slightly more Gaussian PDF, with a less extended tail of overdensities as compared to the lognormal model (see Fig. 4).

We can predict this feature from Fig. 1 in which the gaussianizing transformation grows more slowly at high density than the logarithmic curve and thus will map a larger range of overdensities to an equal sized bin in the transformed field. Since, however, the high-density tail of tracers is best observed and constrained by galaxy counts, the logarithmic model (incorrectly) extrapolates this tail into the underdense regime as enforced by the Gaussian part of the po-

tential Eq. (15). We quantify the \bar{n} dependence of this effect in Fig. 4 and find that one would need an unrealistically high tracer density in order to faithfully reconstruct the one-point statistics of the underlying mass field using the Lognormal function. We can also verify in Fig. 4 that the DoubleLog model does not suffer from this effect and therefore produces a faithful gaussianization at the one point level, independent of \bar{n} . Turning back to Fig. 3, we see that on the level of an individual sample both models are confident in sampling similar structures in overdense regions while for underdense spots the models resort to their gaussian prior and will therefore not be able to predict the filamentary structure by themselves. Finally, for the mean field and its nonlinearized version we again observe a good

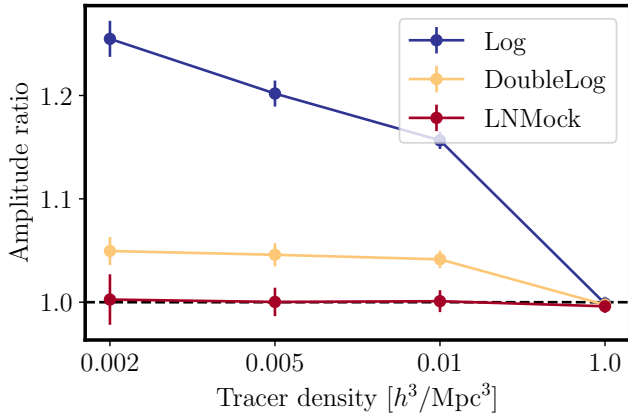


Figure 5. Ratio of the reconstructed power spectrum amplitudes as compared to the best-fit value A^* across the ensemble for different tracer overdensities.

reconstruction of the high ends of the density field while regions with little data information appear washed out.

Due to the (non-Gaussian) filaments in the latent field, we might find that reconstruction with the Gaussian prior of Eq. (10) yields a slightly biased amplitude. In Fig. 5 we quantify the magnitude of this effect and its dependence on the galaxy sampling density on the DoubleLog_BaseRes and Log_BaseRes runs. As a sanity check we also include the lognormal reconstructions LNMock_BaseRes and we find that they give unbiased results, as should occur when the probability being used by the HMC is precisely that from which the data are drawn. We also see that when we assume that the N -body fields are point-transformed Gaussian fields, the DoubleLog transformation produces a much smaller bias on A than the lognormal one. We again attribute this to the DoubleLog transform yielding a better gaussianization of the nonlinear field at the one-point level. The extended underdensity tail that the logarithmic model predicts can only be matched by over-estimating the power spectrum amplitude. The fewer tracers are observed, the more severe this effect and the resulting bias does become. As the DoubleLog model does not suffer from this feature its bias remains nearly constant across all \bar{n} . Repeating the analysis for different gridding scales we find that the bias of the DoubleLog model grows slightly with improving resolution while the logarithmic model is more strongly affected. For both transformations, we find that increasing tracer density lowers the amplitude bias, as the tracers provide stronger constraints on the true mass field and the choice of generative model for δ^{nl} is less important.

Information content

To assess on how much additional information the hierarchical model Eq. (1) contains in comparison to a traditional 2-point analysis, we compare the reconstruction confidence of the power spectrum amplitude chain C_A to the expected variance of the measured power spectra. The first quantity can simply be determined by averaging the signal-to-noise of the C_A over the ensemble,

$$\left(\frac{S}{N}\right)_{\text{hier.}} \equiv \left\langle \frac{\mathbb{E}(C_A)}{\sigma(C_A)} \right\rangle_{\text{chains}}. \quad (18)$$

For obtaining the corresponding measure from the standard analysis we follow the procedure put forward in Rimes & Hamilton (2005);

Lee & Pen (2008) and Neyrinck et al. (2011) and estimate the cumulative information content in the projected power spectra of the untransformed field P about the shot noise subtracted spectra P^{-s} ,

$$\left(\frac{S}{N}\right)^2 (< k) \equiv \sum_{i,j \in \mathcal{R}_k} \left(\frac{P_i^{-s}}{P_i^{-s} + P_i^s} \right) r_{ij}^{-1} \left(\frac{P_j^{-s}}{P_i^{-s} + P_j^s} \right), \quad (19)$$

where P^s denotes the power spectrum induced by the shot noise, r stands for the normalised correlation matrix of P^{-s} and the sum runs over all index pairs for which $k_i, k_j < k$. For a truly Gaussian field with negligible shot noise, the cumulative information is simply the number of 2d Fourier modes available. To minimize the noise when estimating r and therefore get a stable inverse, we obtain this quantity from 2000 Quijote simulations. Those were run on the standard resolution, i.e. using 512^3 dark matter particles and we construct the slabs and tracer counts as described in §2. We include the Hartlap factor (Hartlap et al. 2007) in the computation of the inverse correlation matrix to render it sufficiently unbiased⁵.

In the left hand side of Fig. 6 we compare the two measures Eqs. (18) and (19) for the DoubleLog models of different resolutions at a redshift of $z = 0.5$. Firstly, we see that that the cumulative signal-to-noise of the traditional analysis starts to diverge from the Gaussian scaling at around $k = 0.1 h \text{Mpc}^{-1}$ and quickly plateaus thereafter. In contrast, for the hierarchical model the confidence on the linear amplitude has a significant dependence on the tracer density and resolution and does always yield more information than the power spectrum based method. For a high-sampling limit of $\bar{n} = 1 h^3 \text{Mpc}^{-3}$ Eq. (1) recovers the ideal Gaussian information (mode count) for scales as small as $2 h^{-1} \text{Mpc}^6$. In the upper panel on the right we quantify the information ratio of both analysis methods for $z \in \{0.0, 0.5, 1.0\}$. We see that in addition to increasing the tracer density, additional information can be recovered when reducing the transverse scale of the reconstruction or when using mass fields at a later stage of the cosmic evolution. For example, at $z = 0.5$ the information is at least quadrupled at translinear scales for an attainable shot noise level of $\bar{n} = 0.01 h^3 \text{Mpc}^{-3}$. In the left hand side of Fig. 6 we also show the information of the hierarchical model and the information contained in a discretely sampled Gaussian field,

$$\left(\frac{S}{N}\right)^2 (< k) \equiv \sum_i \frac{N_i}{2} \left(\frac{\bar{n}_{\text{eff},i} P_i}{1 + \bar{n}_{\text{eff},i} P_i} \right)^2, \quad (20)$$

where N_i denotes the number of modes in the corresponding k -bin and for which the (scale dependent) effective sampling density \bar{n}_{eff} is taken to be the inverse of the shot noise spectrum of the transformed field.

In the bottom right panel of Fig. 6 we show the information ratio of the hierarchical model and the discretely sampled Gaussian field. Firstly, we explicitly see that for the highest probed sampling density of tracers the hierarchical model contains the same information as the Gaussian field, which in that case also asymptotes to the mode count limit. Secondly, for the other tracer densities we see that the information ratio appears to increase with improved resolution and it starts being significantly above unity for transverse resolutions of less than $4 h^{-1} \text{Mpc}$, signifying that when using a field based likelihood

⁵ For assessing the impact of the mass resolution of the underlying N -body simulations we repeat the analysis described below using 3000 nearly independent slabs of the 100 Quijote HR simulations that were used for the Hamiltonian reconstruction. The results are fully consistent with the ones presented below.

⁶ In Appendix C we motivate these results from the correlation structure of the spectra of the underlying fields

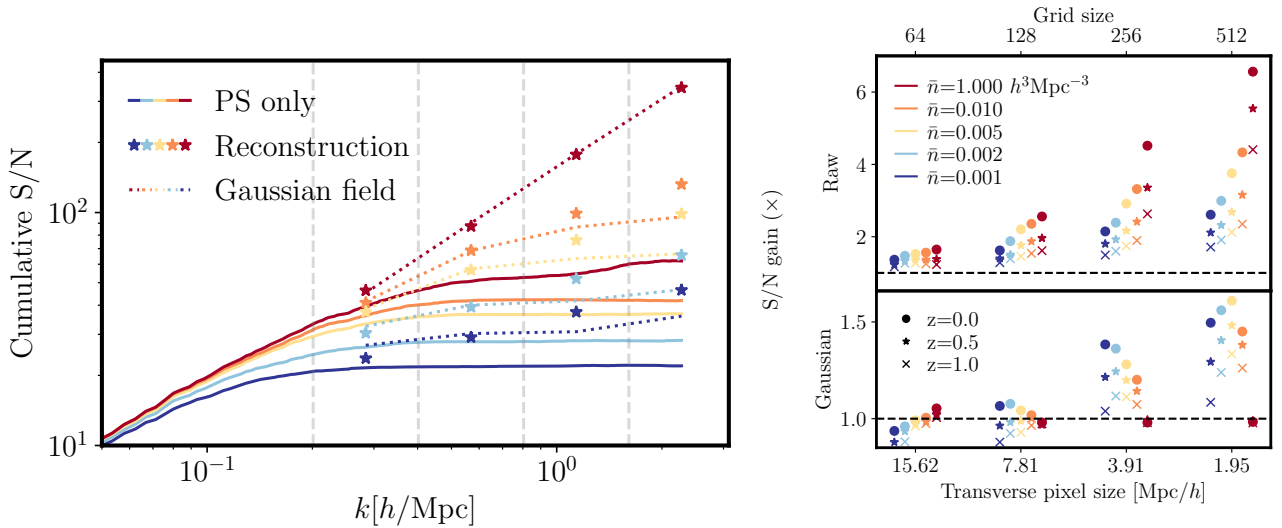


Figure 6. *Left hand side:* Cumulative signal-to-noise ratio on the linear power spectrum amplitude A at $z = 0.5$ when using the power spectrum (solid lines), a Gaussian field with a shot noise contribution matched to the DoubleLog transformation (dashed lines) or the hierarchical model Eq. (1) with the DoubleLog transformation (star markers). The five different colors indicate the sampling densities of the tracers (see legend on the right hand side plot) and the different sets of points correspond to the results when running the reconstruction method on different resolutions, see Table 1 for the details. The grey dashed lines indicate the Nyquist frequencies for each of the probed grid resolutions. *Right hand side:* Signal-to-noise gain of the reconstruction method with respect to the standard analysis in terms of the raw power spectrum (top) and the Gaussian field (bottom) for the three redshifts probed in this work.

one is able to re-capture information that would have otherwise been “lost” in the shot noise. However, we also see that for a very low resolution the hierarchical model seems to contain less information than the Gaussian field. We attribute this to two facts, namely to the slight incorrectness of the point transformation model, as well as to the marginalization over \bar{n} that is implicitly included in Eq. (1).

5 CONCLUSIONS

In this paper we explored the information content of 2d “slabs” of the evolved mass distribution of the universe, when analysed by sampling realizations of this projected mass field from a simple hierarchical model conditioned on the projected galaxy field. The model, described in §2, was composed of a Poisson likelihood for the discrete galaxy distribution and a Gaussian prior on the linearized density field. §3 introduces the HMC sampling algorithm; our implementation choices—namely a sparse non-diagonal mass matrix, a symplectic fourth order integration scheme, and automatic step-size adaptation—yield a feasible and convergent chain for $2 h^{-1} \text{Mpc}$ resolution of a $1 h^{-1} \text{Gpc}$ square slab.

In §4 we showed that the HMC successfully recovers the power spectrum amplitude of lognormal mock catalogs, for which the HMC has the exactly correct probability. Moving to the Quijote N -body simulation suite at $z = 0.5$, for which a linearized Gaussian model is incomplete, we found that there was some bias in the reconstructions, but the DoubleLog function which very nearly Gaussianizes the one-point distribution also recovered the linearized power spectrum with few-percent bias. With high galaxy density (low shot noise), the point-transform reconstruction recovered nearly all of the information on the amplitude, i.e. the Gaussian limit where information equals the mode count, as highlighted in Figures 6 down to resolutions of $2 h^{-1} \text{Mpc}$, whereas the power spectrum captured only the information for scales larger than $\approx 20 h^{-1} \text{Mpc}$, after which it saturates.

In the presence of shot noise, the information in the HMC recon-

struction is of course degraded, but remains 4–5 \times higher than for the power spectrum for sampling densities of $\bar{n} = 0.01 h^3 \text{Mpc}^{-3}$.

This finding suggests that linearization methods proposed for improved information retrieval in spectroscopic galaxy surveys can be applied with substantial benefit to photometric galaxy surveys. This HMC field-sampling method can be extended to multiple line-of-sight slabs, and it will be straightforward to add the probability of weak lensing shear or convergence observations to the hierarchical model. Thus in future work we will develop techniques for replacing the “3 \times 2-point” data vectors that are now the standard for cosmological analyses of lensing+galaxy surveys with field sampling that yields much more precision from the same data.

Before closing we recall that the model presented in this work was intended to be idealized such that the computational cost for getting reasonable estimates of the information recovered by our field based reconstruction method was feasible. For obtaining robust cosmological constraints one needs to refine some modelling choices; i.e. include a different (yet still deterministic) model for structure formation, a power spectrum model obtained from a differentiable Boltzmann solver, and potentially also some modifications to the Poisson assumption for the sampling of tracers (?). We expect that the information content of such a model will still be comparable to the results found in this work and therefore yield more information than a traditional analysis.

ACKNOWLEDGEMENTS

We thank the anonymous referee for helpful comments. LP acknowledges support from a STFC Research Training Grant (grant number ST/R505146/1) and from the DLR grant 50QE2002. GMB acknowledges support for this work from US Department of Energy grant DE-SC00079014 and National Science Foundation grant AST-2009210. RES acknowledges support from the STFC (grant number ST/P000525/1, ST/T000473/1). This work used the DiRAC@Durham facility managed by the Institute for Computa-

tional Cosmology on behalf of the STFC DiRAC HPC Facility (www.dirac.ac.uk). The equipment was funded by BEIS capital funding via STFC capital grants ST/K00042X/1, ST/P002293/1, ST/R002371/1 and ST/S002502/1, Durham University and STFC operations grant ST/R000832/1. DiRAC is part of the National eInfrastructure. This research made use of numpy, a library used for scientific computing and technical computing and matplotlib, a Python library for publication quality graphics (Harris et al. 2020; Hunter 2007).

DATA AVAILABILITY

Instructions on how to access and download the data of the Quijote Simulation suite can be found in <https://github.com/franciscovillaescusa/Quijote-simulations>. Additional data underlying this article will be shared on reasonable request to the corresponding author.

REFERENCES

- Atchadé Y. F., Rosenthal J. S., 2005, *Bernoulli*, 11, 815
- Betancourt M., 2016, arXiv e-prints, p. [arXiv:1601.00225](https://arxiv.org/abs/1601.00225)
- Betancourt M., 2017, arXiv e-prints, p. [arXiv:1701.02434](https://arxiv.org/abs/1701.02434)
- Creutz M., Gocksch A., 1989, *Phys. Rev. Lett.*, 63, 9
- Duane S., Kennedy A., Pendleton B. J., Roweth D., 1987, *Physics Letters B*, 195, 216
- Gelman A., Rubin D. B., 1992, *Statistical Science*, 7, 457
- Giblin B., et al., 2018, *MNRAS*, 480, 5529
- Harris C. R., et al., 2020, *Nature*, 585, 357
- Hartlap J., Simon P., Schneider P., 2007, *A&A*, 464, 399
- Hernández-Sánchez M., Kitaura F.-S., Ata M., Dalla Vecchia C., 2021, *MNRAS*, 502, 3976
- Hoffman M. D., Gelman A., 2014, *Journal of Machine Learning Research*, 15, 1593
- Hunter J. D., 2007, *Computing in Science & Engineering*, 9, 90
- Jasche J., Kitaura F. S., 2010, *MNRAS*, 407, 29
- Jasche J., Wandelt B. D., 2013, *MNRAS*, 432, 894
- Jasche J., Leclercq F., Wandelt B. D., 2015, *J. Cosmology Astropart. Phys.*, 2015, 036
- Joachimi B., Taylor A. N., Kiessling A., 2011, *MNRAS*, 418, 145
- Kitaura F. S., Enßlin T. A., 2008, *MNRAS*, 389, 497
- Lavaux G., Jasche J., 2016, *MNRAS*, 455, 3169
- Layzer D., 1956, *AJ*, 61, 383
- Leclercq F., Heavens A., 2021, *MNRAS*, 506, L85
- Leclercq F., Jasche J., Lavaux G., Wandelt B., Percival W., 2017, *J. Cosmology Astropart. Phys.*, 2017, 049
- Lee J., Pen U., 2008, *ApJ*, 686, L1
- Leimkuhler B. J., Reich S., 2004, *Simulating Hamiltonian dynamics*. Cambridge monographs on applied and computational mathematics, Cambridge Univ., Cambridge, <https://cds.cern.ch/record/835066>
- McLachlan R., 1995, *SIAM J. Sci. Comp.*, 16, 151
- Neal R. M., 2012, arXiv e-prints, p. [arXiv:1206.1901](https://arxiv.org/abs/1206.1901)
- Nesterov Y., 2009, *Mathematical Programming*, 120, 221
- Neyrinck M. C., Szapudi I., Szalay A. S., 2009, *ApJ*, 698, L90
- Neyrinck M. C., Szapudi I., Szalay A. S., 2011, *ApJ*, 731, 116
- Peebles P. J. E., 1980, *The large-scale structure of the universe*. Research supported by the National Science Foundation. Princeton, N.J., Princeton University Press, 1980. 435 p.
- Porqueres N., Heavens A., Mortlock D., Lavaux G., 2021, arXiv e-prints, p. [arXiv:2108.04825](https://arxiv.org/abs/2108.04825)
- Rimes C. D., Hamilton A. J. S., 2005, *MNRAS*, 360, L82
- Robbins H., Monro S., 1951, *Annals of Mathematical Statistics*, 22, 400
- Seo H.-J., Sato M., Dodelson S., Jain B., Takada M., 2011, *ApJ*, 729, L11
- Simpson F., Heavens A. F., Heymans C., 2013, *Phys. Rev. D*, 88, 083510
- Simpson F., Harnois-Déraps J., Heymans C., Jimenez R., Joachimi B., Verde L., 2016, *MNRAS*, 456, 278
- Villaescusa-Navarro F., et al., 2020, *ApJS*, 250, 2
- Wang H., Mo H. J., Yang X., Jing Y. P., Lin W. P., 2014, *ApJ*, 794, 94
- Yoshida H., 1990, *Physics Letters A*, 150, 262

APPENDIX A: DETAILS OF THE IMPLEMENTATION

A1 Choice of mass matrix

The mass matrix can be written in a block like structure consisting of the Hessian associated with the latent field parameters, the Hessian with respect to the power spectrum amplitude, and a mixed one. For this work we make the following choices:

$$\begin{aligned} \mathbf{M} &= \begin{bmatrix} \nabla_{\vec{\delta}}^2 (\psi_{\text{Pois}} + \psi_{\text{Gauss}}) & \nabla_{\vec{\delta}, \vec{\Pi}_{P^*}}^2 \psi_{\text{Gauss}} \\ \nabla_{\vec{\delta}, \vec{\Pi}_{P^*}}^2 \psi_{\text{Gauss}} & \nabla_{\vec{\Pi}_{P^*}}^2 \psi_{\text{Gauss}} \end{bmatrix} \\ &\equiv \begin{bmatrix} \nabla_{\vec{a}}^2 \psi_{\text{Gauss}} + \vec{\varepsilon} & -\frac{\partial \vec{P} / \partial \vec{\Pi}_{P^*}}{(\vec{P}^*)^{3/2}} \\ -\frac{\partial \vec{P} / \partial \vec{\Pi}_{P^*}}{(\vec{P}^*)^{3/2}} & \frac{1}{2} \frac{\partial \vec{P} / \partial \vec{\Pi}_{P^*}}{\vec{P}^*} \cdot \frac{\partial \vec{P} / \partial \vec{\Pi}_{P^*}}{\vec{P}^*} \end{bmatrix} \\ &= \begin{bmatrix} \frac{1}{\vec{P}^*} (\vec{1} + \vec{P}^* \odot \vec{\varepsilon}) & -\frac{1}{A^* \sqrt{\vec{P}^*}} \\ -\left(\frac{1}{A^* \sqrt{\vec{P}^*}}\right)^T & \frac{n_L}{2A^{*2}} \end{bmatrix}, \end{aligned} \quad (\text{A1})$$

where in the first step we drop the Poisson contribution, introduce a positive definite, constant normalization vector $\vec{\varepsilon}$ that is needed to keep the mass well defined, and substitute the Fourier space representation of Eq. (10) evaluated at $a^\dagger a = P^*$. In the second step we specialize to the case in which $\vec{\Pi}_{P^*} \equiv A^*$ and introduce the symbol \odot to denote the Hadamard product. As the latent part has a diagonal structure we can easily compute the inverse with help of the block matrix inversion formula:

$$\begin{aligned} \mathbf{M}^{-1} &= \begin{bmatrix} \left(\sqrt{\vec{P}^*} \odot \vec{X}\right) \mathbb{1} + \alpha \vec{X} \otimes \vec{X} & \alpha A^* \vec{X} \\ \alpha A^* \vec{X}^T & \alpha A^{*2} \end{bmatrix}, \\ \text{where } \vec{X} &\equiv \frac{\sqrt{\vec{P}^*}}{\vec{1} + \vec{P}^* \odot \vec{\varepsilon}} \quad \alpha \equiv \frac{2}{n_L} \frac{1}{1 - 2 \left\langle \frac{1}{1 + \vec{P}^* \odot \vec{\varepsilon}} \right\rangle}. \end{aligned} \quad (\text{A2})$$

To circumvent the large storage requirements of this representation we make use the fact that we only need to perform the operation $\mathbf{M}^{-1} \vec{p}$ within the integrator which can be done in linear time and space complexity as

$$\mathbf{M}^{-1} \begin{bmatrix} \vec{p}_L \\ \vec{p}_{\vec{\Pi}} \end{bmatrix} = \begin{bmatrix} \sqrt{\vec{P}^*} \odot \vec{X} \odot \vec{p}_L + \alpha \Sigma \vec{X} + \alpha A^* p_{\vec{\Pi}} \vec{X} \\ \alpha A^* \Sigma + A^{*2} \alpha p_{\vec{\Pi}} \end{bmatrix}, \quad (\text{A3})$$

where we defined $\Sigma \equiv \vec{X}^T \cdot \vec{p}_L$. We can now draw a random momentum vector as follows:

(i) Compute a lower triangular matrix \mathbf{L} s.t. $\mathbf{M} = \mathbf{L}\mathbf{L}^T$. In our case the resulting Cholesky matrix reads

$$\mathbf{L} = \begin{bmatrix} \frac{1}{\sqrt{\vec{P}^*}} \sqrt{\vec{1} + \vec{P}^* \odot \vec{\varepsilon}} & 0 \\ -\left(\frac{\vec{X}}{A^* \sqrt{\vec{P}^*}}\right)^T & \frac{1}{\sqrt{\alpha A^*}} \end{bmatrix}. \quad (\text{A4})$$

(ii) Draw a random unit Gaussian, $\vec{z} \sim \mathcal{H}(0, \mathbb{1}_{n_L}) \otimes \mathcal{G}(0, 1)$, where for the latent field pixels we enforce hermitian symmetry.

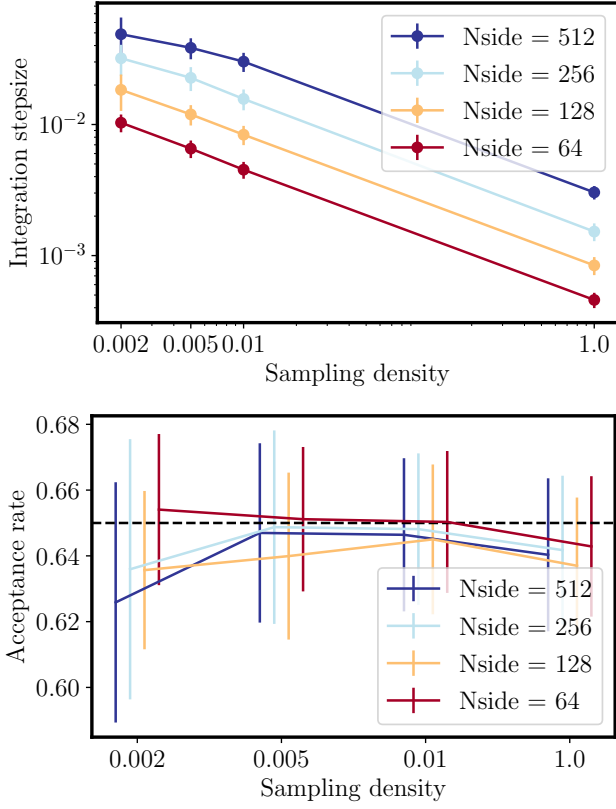


Figure A1. *Upper panel:* The final step-size proposed by the dual averaging algorithm for the DoubleLog models. *Lower panel:* Mean acceptance rate of the chains during the sampling stage. The black dashed line indicates the target acceptance rate of $\delta \equiv 0.65$ used within the dual averaging algorithm. For both plots we took into account all the chains in the DoubleLog models and averaged over all the seeds.

(iii) Transform z to inherit the correct covariance properties: $\vec{p} = \mathbf{L}\vec{z}$. This can again be done without needing to store \mathbf{L} as a whole.

A2 Dual Averaging

We implement a dual averaging algorithm using the same formalism as presented in Hoffman & Gelman (2014), see their Algorithm 5 for the specific implementation and initialization values. At its core, their dual averaging algorithm aims at dynamically adjusting the step-size ϵ of the chain during burn-in such that some target acceptance rate δ is reached, where δ should be chosen to maximize the trajectory length (i.e. lowering the correlation between subsequent samples) while keeping the rejection rate sufficiently low. Compared to traditional adaptation methods (Robbins & Monro 1951; Atchadé & Rosenthal 2005) the dual averaging method does give a larger weight to more recent iterations and therefore allows for a quicker convergence to the ‘optimal’ step-size. As our target acceptance rate we chose $\delta = 0.65$ as proposed by Hoffman & Gelman (2014). In Fig. A1 we show how well this setup did work in the ensemble runs which were all starting the first burn-in stage with the same, very small step-size. We see that the resulting step-size is indeed compatible with the target acceptance rate for all the probed ensemble runs. We also see that there is a strong dependence of the inferred step-size on the galaxy sampling density and the pixel scale. However, we also find that for this automatically inferred step-size there is a non-negligible amplitude bias present in

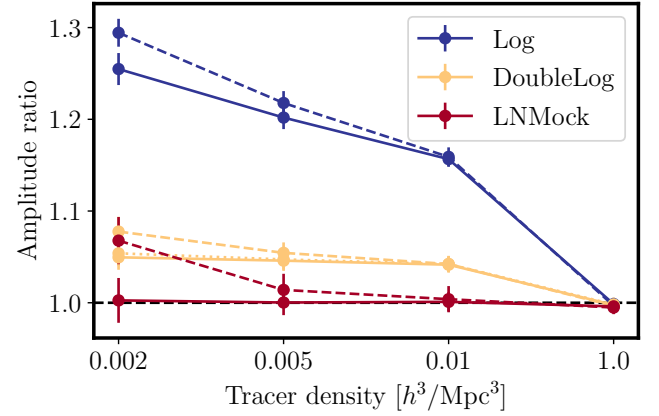


Figure A2. Dependence of the power spectrum amplitude ratio on the target acceptance rate δ in the dual averaging algorithm for different transformations in the ensemble runs performed on a 256^2 grid. The solid lines display the results for $\delta = 0.95$ using the fourth order integrator while for the dashed lines we choose $\delta = 0.65$ and use the Leapfrog integration routine. The yellow dotted line corresponds to an ensemble run using the Leapfrog integrator with $\delta = 0.95$.

the lognormal mocks for a very low galaxy sampling density. When using a much more restrictive value of $\delta = 0.95$ in the dual averaging algorithm we find that this bias disappears. In Fig. A2 we compare the amplitude biases resulting from the different choices of δ for the Quijote snapshots and see that the most significant differences occur for small tracer densities. We note that the necessity of accepting nearly all proposed samples leads to the increased efficiency of the fourth order integrators compared to the Leapfrog routine as the former ones are not as strongly affected by the choice of δ . Finally, we remark that the choice of δ does not significantly affect our estimate of the reconstruction confidence.

A3 Symplectic integrators

In a more compact form the Hamilton equations of motion Eq. (14) can be written in terms of the phase space variable $\vec{z} \equiv (\vec{q}, \vec{p})$ and the Poisson bracket $\{\cdot, \cdot\}$ as

$$\frac{d}{dt} \vec{z} \equiv -\{\mathcal{H}, \vec{z}\}. \quad (\text{A5})$$

We furthermore introduce the flow map ϕ_t which evolves some initial condition \vec{z}_0 along the Hamiltonian trajectory; the underlying geometry of Hamiltonian dynamics then demands that the flow map is a symplectomorphism such that we also need to embed the properties of this feature into our numerical approximation of the true flow.

Treating the Poisson bracket as a differential operator, $\{X, Y\} \equiv D_Y X$, we can formally solve Eq. (A5) using an exponential:

$$\vec{z}(t) = \exp(D_{\mathcal{H}t}) \vec{z}(0) \equiv \exp[(D_\psi + D_T)t] \vec{z}(0), \quad (\text{A6})$$

where we split the operator in its Potential (D_ψ) and kinetic (D_T) parts. On their own, the individual summands update the phase space vector by discretely evolving (translating) the Hamiltonian equations of motion Eq. (14) for a single time step ϵ :

$$\begin{aligned} e^{D_T \epsilon} &\equiv \mathcal{T}_{\vec{p}}(\epsilon) : (\vec{q}, \vec{p}) \rightarrow (\vec{q} + \epsilon M^{-1} \vec{p}, \vec{p}), \\ e^{D_\psi \epsilon} &\equiv \mathcal{T}_{\vec{q}}(\epsilon) : (\vec{q}, \vec{p}) \rightarrow (\vec{q}, \vec{p} - \epsilon \nabla_{\vec{q}} \psi). \end{aligned} \quad (\text{A7})$$

In order to construct an n th order explicit discretisation scheme we

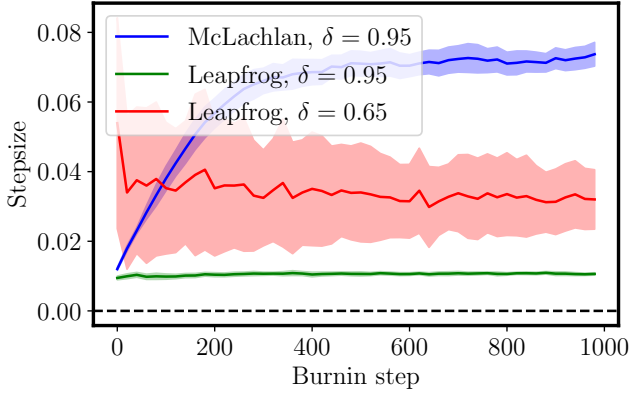


Figure A3. Comparison of the integration step-size evolution during the burnin stage for the second and fourth order integrators across the corresponding ensembles using 256^2 grids. As we only store thinned chains for those measurements the curves appear slightly discontinuous.

need to find an approximate solution up to an error $O(t^n)$ in which the two differential operators are split:

$$\exp[(D_\psi + D_T)t + O(t^n)] = \prod_{i=1}^k \exp(c_i D_\psi t) \exp(d_i D_T t) + O(t^n). \quad (\text{A8})$$

Finding a set of algebraic requirement on the coefficients to guarantee an integrator of order n can be achieved by making use of the Baker-Campbell-Hausdorff formula that can be repeatedly applied to yield:

$$e^X e^Y e^X = e^W : W = 2X + Y + \frac{1}{6}[Y, [Y, X]] - \frac{1}{6}[X, [X, Y]] + \dots \quad (\text{A9})$$

As the most simple example we can verify the discretisation scheme used in the Leapfrog integrator:

$$\begin{aligned} \phi_\epsilon^{(\text{lf})} &= e^{c_1 D_\psi \epsilon} e^{d_1 D_T \epsilon} e^{c_1 D_\psi \epsilon} + O(\epsilon^3) \equiv e^{(D_\psi + D_T)\epsilon + O(\epsilon^3)} \\ &\Rightarrow \phi_\epsilon^{(\text{lf})} = \mathcal{T}_{\bar{p}}(\epsilon/2) \mathcal{T}_{\bar{q}}(\epsilon) \mathcal{T}_{\bar{p}}(\epsilon/2). \end{aligned} \quad (\text{A10})$$

For obtaining higher order integrators one needs to chain together more individual updates. In order to find locally optimal solutions for the coefficients one usually opts for sufficiently many updates, such that in addition to the algebraic constraints the remaining coefficients can be chosen by optimizing certain quantities, such as leading order terms in the error expansion. In particular, the fourth order integrator of McLachlan (1995) is obtained by symmetrically concatenating five Leapfrog routines using different weights:

$$\phi_\epsilon^{(\text{mcl})} = \phi_{w_1 \epsilon}^{(\text{lf})} \circ \phi_{w_2 \epsilon}^{(\text{lf})} \circ \phi_{w_3 \epsilon}^{(\text{lf})} \circ \phi_{w_2 \epsilon}^{(\text{lf})} \circ \phi_{w_1 \epsilon}^{(\text{lf})}, \quad (\text{A11})$$

where the optimal weights are given as $w_1 = 0.28$, $w_2 = 0.62546642846767004501$ and $w_3 = 1 - 2(w_1 + w_2)$. A naive implementation of this method will require 15 single updates per integration step. However, we can reduce this number by making use of the fact that the position vector is not affected in the momentum update; this allows us to concatenate the momentum updates in between adjacent leapfrog steps. Note that when evolving an initial state for $m > 1$ time steps ϵ it is possible to further reduce the number of operations by additionally chaining together the final momentum updates in between steps. If an integrator x requires $n_x^{(1)}$ stages for a

single time step the full evolution can be obtained using

$$n_x^{(m)} = n_x^{(1)} + (m-1) \left(n_x^{(1)} - 1 \right) \xrightarrow{m \gg 1} m \left(n_x^{(1)} - 1 \right)$$

single updates. For the Leapfrog integrator and the fourth integrator of (McLachlan 1995) we have $n_{\text{lf}}^{(1)} = 3$ and $n_{\text{mcl}}^{(1)} = 11$ such that the fourth order integrator asymptotes to requiring five times more time than the leapfrog routine. In Fig. A3 we show the difference of the inferred step-size for the Leapfrog and fourth order integrator and we infer that for such model specifications a speedup of around 50% can be expected during the sampling phase.

We postpone a more thorough investigation of the applicability and performance of various other higher order integration schemes to future work. For additional details on numerical Hamiltonian dynamics we refer the reader to Leimkuhler & Reich (2004).

APPENDIX B: CONVERGENCE TESTS

In Fig. A4 we show the potential scale reduction factor (PSFR) of the Gelman-Rubin diagnostics (Gelman & Rubin 1992) for the DoubleLog_BaseRes and the DoubleLog_BaseResrun_mcl runs. We see that the amplitude chains did converge for practically all the runs, except for some reconstructions performed with very low galaxy sampling densities in the leapfrog case. However, as those PSFR values are only slightly above the 1.1 level and we just care about the ensemble mean of the distributions, this should not pose a problem. For the latent pixel parameters we see that the mean PSFR for all the runs is very well consistent with unity which signifies convergence of the individual chains. Performing Gelman-Rubin diagnostics on the other ensemble runs we find similar results.

APPENDIX C: CORRELATION MATRICES OF THE PROJECTED FIELDS

In Fig. C1 we show the correlation structure of the power spectra of the three projected fields discussed in this work, namely the untransformed field, the log-transformed field and the DoubleLog-transformed field for their base resolution of $\approx 4 h^{-1} \text{Mpc}$. We see that on small scales ($k \gtrsim 0.3 h \text{Mpc}^{-1}$) there is significant mode coupling in the spectra of the untransformed field while the correlation matrix of the spectra of the transformed fields exhibit a nearly diagonal structure. Thus, we expect the information content of the raw field to deplete relative to a Gaussian field at those scales and to reach a plateau in the high- k regime. In contrast, for both of the transformed fields there is no significant mode coupling at any scale probed in this work such that these fields contain a similar amount information as a Gaussian field.

This paper has been typeset from a $\text{\TeX}/\text{\LaTeX}$ file prepared by the author.

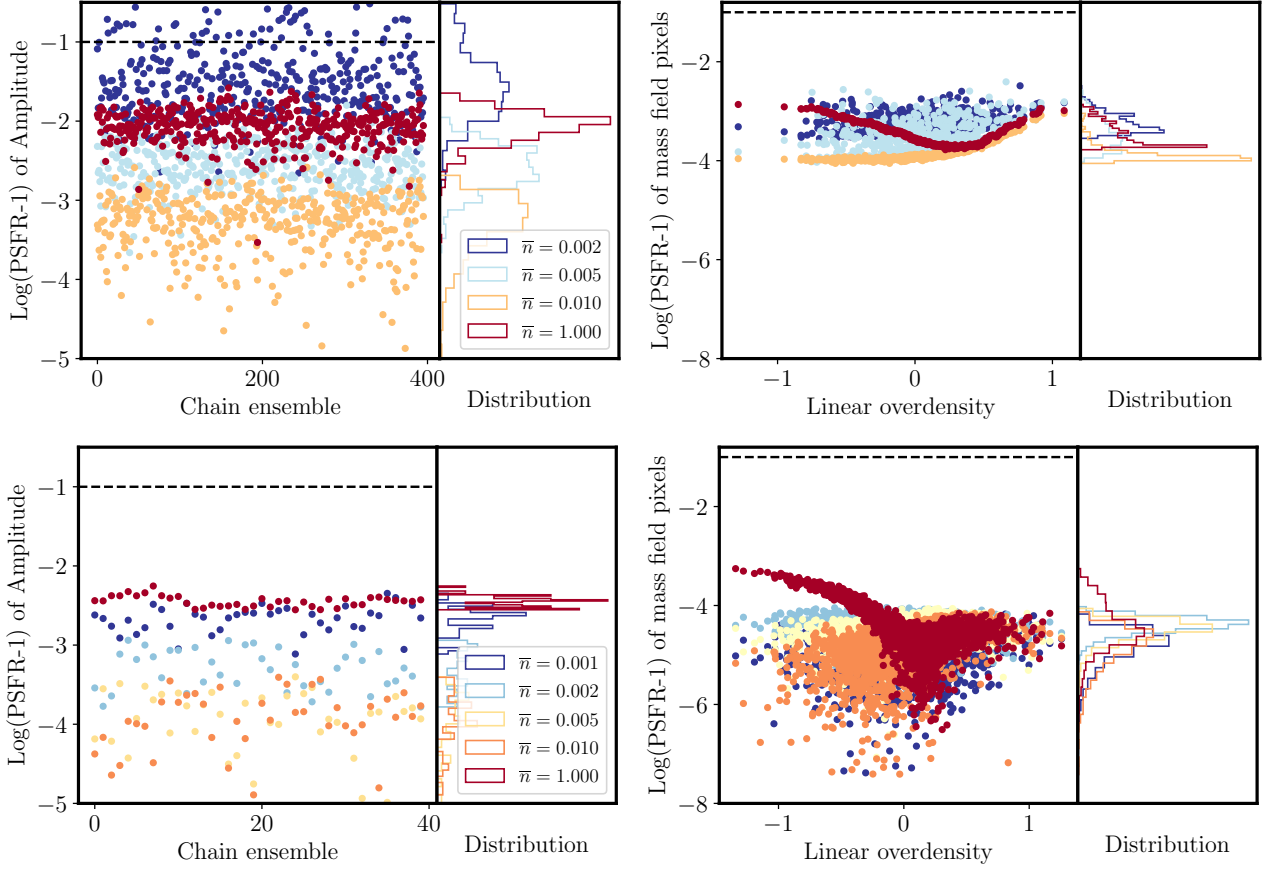


Figure A4. Convergence diagnostic of the chains in the Quijote baseline ensemble run (top) and the corresponding run using the fourth order integrator (bottom). The left hand side shows the results for the power spectrum amplitude for each of the individual runs. The color coding corresponds to the different galaxy sampling densities. On the right hand side we plot the ensemble mean of the PSFR for 500 (top) and 2000 (bottom) randomly chosen pixels. In each panel the dashed black line indicates the boundary of our chosen measure of convergence; point below this line signify a set of chains that have converged.

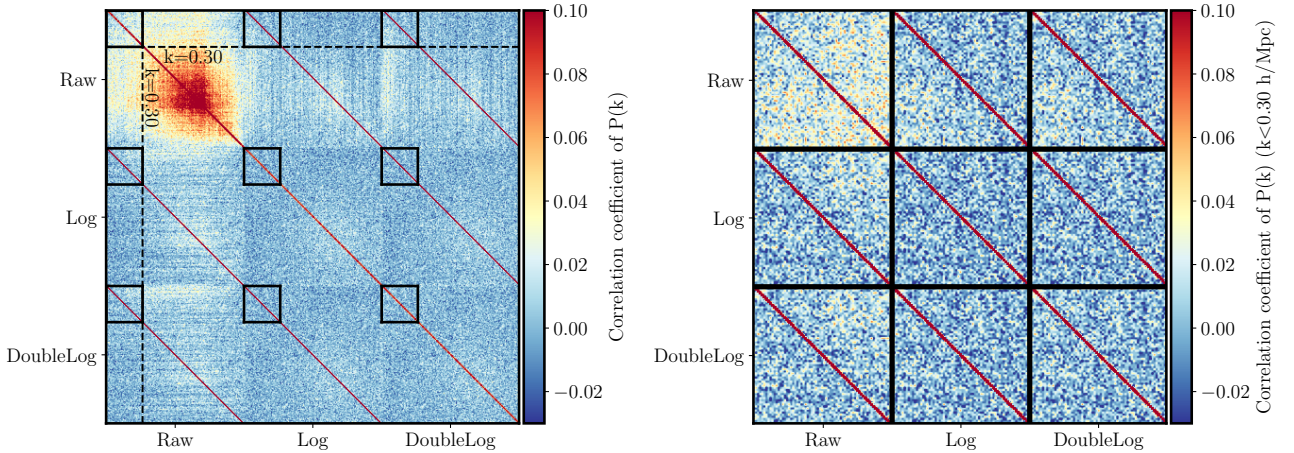


Figure C1. *Left hand side:* Correlation matrices of the power spectra for the nonlinear field and its two transformations used in this work (transverse resolution $\approx 4 h^{-1} \text{Mpc}$). *Right hand side:* Correlation matrix of the blocks with $k < 0.30 h \text{Mpc}^{-1}$. For those scales there is only a slight amount of mode coupling present in the spectra of the raw field s.t. the information content will be only depleted by a bit with respect to the Gaussian limit.